# Notes and Illustrations for Weakly Diverging to Tightly Focused Gaussian Beams

*Uri Levy*[*] *and Yaron Silberberg*
*Weizmann Institute of Science, Rehovot 7610001, Israel*
**Corresponding author: uri.levy@weizmann.ac.il*

Published 19 August 2016

**A JOSA A published article by the name *Weakly Diverging to Tightly Focused Gaussian Beams: a Single Set of Analytic Expressions* brings, as the name suggests, analytic expressions for Gaussian beams, to high order in divergence angle. To keep the article short and concise, some properties of the Gaussian beams were discussed very briefly or not discussed at all. Here we write notes and bring additional illustrations to make the entire description of the Gaussian beams more complete. Importantly, we show here curves of strict power conservation along the propagation axis for both linearly polarized and radially polarized Gaussian beams when such beams are described by the presented analytic expressions.**

***OCIS codes:*** *(260.2110) Electromagnetic optics; (070.7345) Wave propagation*

## 1. Notes related to the recursive relations

Notes related to the recursive relations ([48] Eq. (10)).

(1) We have added a multiplicative constant ($A_0$) to the solution of the homogeneous equation for the zero-order envelope function ($\psi_0(x,y,z)$ – [48] Eq. (14)). Later on we have defined this $A_0$ constant as

$$A_0 \equiv \frac{E_0}{\mathbb{i}\cdot k_0} \tag{S1}$$

in order to get electric-magnetic field units ($E_0$) for both the electric field components $\mathbb{E}(r)$ and for the magnetic field components $\mathbb{B}(r)$ (cf. [48] Eq. (2), cgs units).

(2) The wavenumber of the time-harmonic fields ([48] $k_H$ – Eq. (1)) can in general be complex (i.e. include a loss term). Following Stratton ([1], page 392), the wave number can generally be defined as (see [1] for the definition of the parameters, MKS units):

$$k_H^2 = \epsilon\cdot\mu\cdot\omega^2 + \mathbb{i}\cdot\sigma\cdot\mu\cdot\omega \tag{S2}$$

(3) Looking at the recursive relations for the vector potential's envelope functions ([48] Eq. (10)), we see that each function $\psi_n(x,y,z)$ plays the role of a source polarization density for the next function $\psi_{n+2}(x,y,z)$. Perhaps it makes sense then to conceptualize a physical process where a Gaussian beam (in vacuum or in a medium) is built up (infinitely quickly) by sequentially generated envelope functions (each with its correct weight).

## 2. Linearly polarized Gaussian fields – illustrating maps

See the main article for the following figures and tables:

**FIG. 1.** Parameters of a Gaussian beam.
**FIG. 2.** Electric field components of an *x* -polarized Gaussian beam.
**FIG. 3.** Magnetic field components of an *x* -polarized Gaussian beam.
**FIG. 4.** High divergence-angle electric fields.
**TABLE I.** Expressions for the field components of a linearly polarized Gaussian beam.
**TABLE II.** Expressions for the field components of a radially polarized Gaussian beam (cylindrical coordinates).
**TABLE III.** Expressions for the field components of a radially polarized Gaussian beam (Cartesian coordinates).

Next, **FIG. S5** shows intensity flow of the Gaussian beam components, as calculated by the time-averaged Poynting vector - $\boldsymbol{S}_{avg}(x,y,z)$ ([1], Sec. 2.21, pp. 137, Eq. 29, here in cgs units):

$$\boldsymbol{S}_{avg}(x,y,z) = \frac{1}{2}\cdot\frac{c}{4\cdot\pi}\cdot Re\left[\boldsymbol{E}(x,y,z,t)\times\boldsymbol{B}^*(x,y,z,t)\right] \tag{S3}$$

Top row shows cross-sectional maps at $z_{plot} = 100\mu m$ and bottom row shows axial maps in the *x*-*z* plane or the *y*-*z* plane. Erikson and Singh presented a ray picture of a Gaussian beam's power flow, clearly showing the pre-focus inwards flow and the post-focus outwards flow [8].

Expression 1 of **TABLE I** for the zero-order *x* component of the electric field, includes a $x^2$ term. As the term grows with diffraction angle, we expect to see some ellipticity of the Gaussian beam at large diffraction angles. This indeed is the case as shown by **FIG. S6**. Top row – cross-sections at the focal plane ($z_{plot} = 0$). The electric field is seen to be elliptical with the long axis parallel to the *x* axis (the axis of polarization). The magnetic field (*y* component of) is circular (as a result of the assumption of a single component vector potential). The axial component of the Poynting vector is still elliptical with lower eccentricity (vs. the eccentricity of the electric field's cross-section). Similarly, ellipticity of $E_x$ is predicted at a distance

(bottom row, $z_{plot} = 100\mu m$), only this time, as the beam diffracts, the long axis lies in the $y$ direction (perpendicular to the electric-field's polarization).

Next figure in this section, **FIG. S7**, illustrates the improvement in solving Helmholtz equation ([48] Eq. (1)) when the second-order term is added to the zero-order term of the vector potential ([48] Eq. (15)). The improvement is extended to each and every component of the derived electric-magnetic fields. The figure shows a map of the two-term potential ([48] Eq. (15)), along with two Helmholtz equation residue maps (Eq. (S4)). One residue map $H_0^{LNR}(x,y,z)$ for Helmholtz equation applied to the zero-order vector potential only (top of Eq. (S4)) and another residue map $H_{all}^{LNR}(x,y,z)$ for the zero-order and the correcting second-order term together (bottom of Eq. (S4)).

$$H_0^{LNR}(x,y,z) = \nabla^2\left[\psi_0(x,y,z)\cdot e^{i\cdot k_H\cdot z}\right] + k_H^2\cdot\left[\psi_0(x,y,z)\cdot e^{i\cdot k_H\cdot z}\right]$$
$$H_{all}^{LNR}(x,y,z) = \nabla^2\left\{\left[\psi_0(x,y,z) + \theta_d^2\cdot\psi_2(x,y,z)\right]\cdot e^{i\cdot k_H\cdot z}\right\}$$
$$+k_H^2\cdot\left\{\left[\psi_0(x,y,z) + \theta_d^2\cdot\psi_2(x,y,z)\right]\cdot e^{i\cdot k_H\cdot z}\right\} \qquad \textbf{(S4)}$$

At the angle-axial distance for which the maps are calculated ([48] Eq. (20)), the two-term vector potential is more accurate (vs. the zero-order term only) and the residue of Helmholtz equation applied to the two-term vector potential (at the shown axial distance) is visibly smaller.

The two maps of **FIG. S8** display the electric-field $x$-component ($E_x$ at the focal plane of a high divergence-angle Gaussian beam ($\theta_d = 37^0 \Rightarrow w_0 = 0.5\mu m$). A weak ring (predicted by the expression of **TABLE I**) shows up around the main spot. Similar rings show up also for the other field components. Note that these rings are predicted by the analytic expressions and are not a result of a limiting aperture.

Last figure in this section, **FIG. S9**, displays a distribution map of the angle between the electric-field vector and the magnetic-field vector. Generally, free-medium electromagnetic waves are not necessarily perpendicular [46]. This indeed is the case with the linearly polarized Gaussian beam (when all field components, as in **TABLE I**, are included). The electric-magnetic fields of a linearly polarized Gaussian beam are generally non-perpendicular at all divergence angles and at all axial distances, including $z = 0$, i.e. including the focal plane.

The angles between $\boldsymbol{E}$ and $\boldsymbol{B}$ are calculated according to:

$$\theta[deg.] = \left(\frac{180}{\pi}\right)\cdot\cos^{-1}\left(\frac{Re\left[\boldsymbol{E}(x,y,z)\circ\boldsymbol{B}^*(x,y,z)\right]}{\left|\boldsymbol{E}(x,y,z)\right|\cdot\left|\boldsymbol{B}(x,y,z)\right|}\right) \qquad \textbf{(S5)}$$

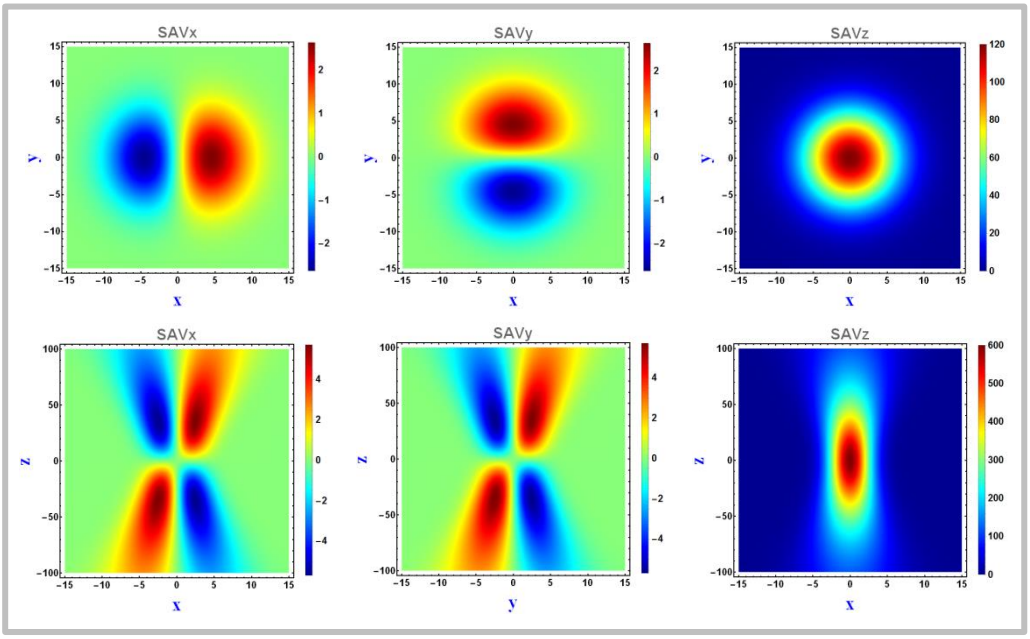


**FIG. S5.** Intensity flow ($\boldsymbol{S}_{avg}^{LNR}(x,y,z)$) of a linearly polarized Gaussian beam. The maps were calculated for the full field expressions and thus are (slightly) more accurate (vs. the zero-order-only maps). (see [8], fig. 1 for a ray picture of intensity flow). Values of the color scales were calculated for $C_{light} = 1$.

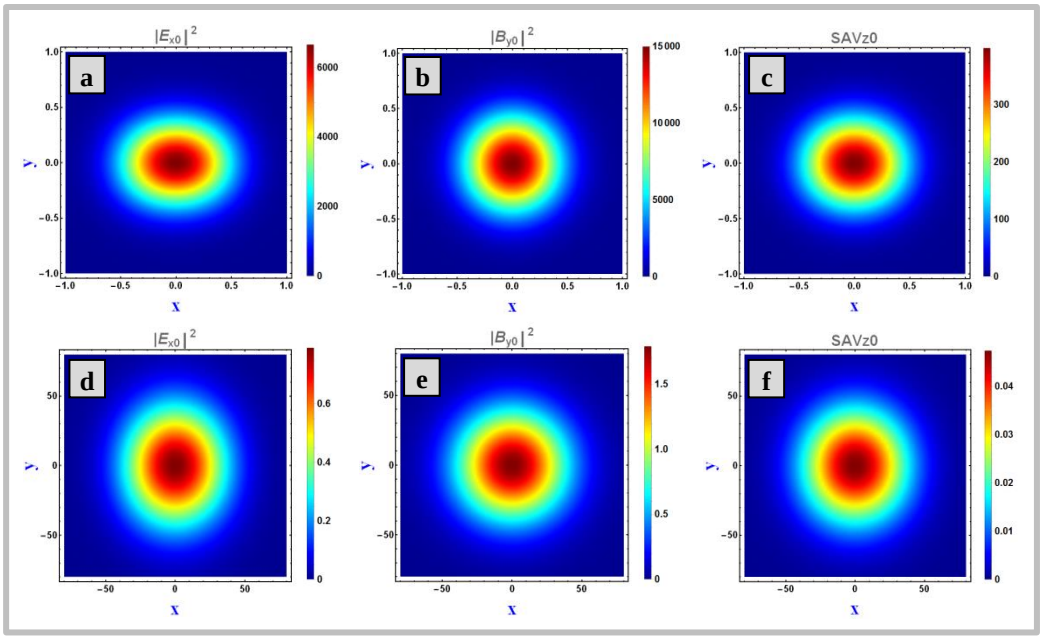


**FIG. S6.** Zero-order only $x$-component of the linearly polarized Gaussian beam ($\mathbb{E}_{x0}^{LNR}$) at a large divergence angle of $\theta_d = 34.8^0$ (cf. expression 1 of **TABLE I**). Top row: $z_{plot} = 0$ Bottom row: $z_{plot} = 100\mu m$. **a**,**d** – $x$-component of the electric field, showing elliptical spot. Note in **d** the $90^0$ rotation of the ellipse due to diffraction. **b**,**e** – $y$-component of the magnetic field ($\mathbb{B}_{y0}^{LNR}$), showing a circular spot (cf. expression 10 of **TABLE I**). **c**,**f** – $z$-component of the time-averaged Poynting vector, still showing some ellipticity. According to **[9]**, **[17]**, and **[38]**, $\mathbb{B}_{y0}^{LNR}$ is also elliptic (with the ellipse rotated by $90^0$ relative to the $\mathbb{E}_{x0}^{LNR}$ ellipse).

$\{\lambda_0 = 1.551\mu m\ ; n = 1.507\ ; w_0 = 0.54\mu m\ ; z_R = 0.89\mu m\ ; \theta_d = 34.8^0\}$.

---

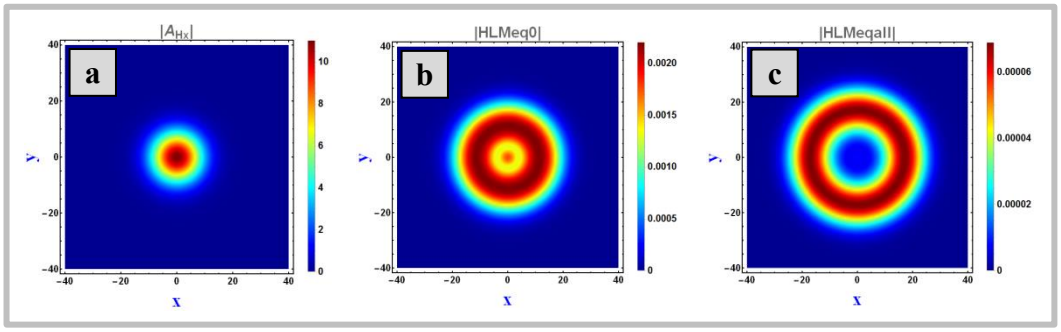


**FIG. S7.** Improvement of the solution to Helmholtz equation for the single component vector potential. **a** – map of the two-term single component vector potential (absolute value of). **b** – residue of Helmholtz equation applied to the zero-order vector potential only (top of Eq. **(S4)**). **c** - residue of Helmholtz equation applied to the two orders vector potential (bottom of Eq. **(S4)**). Looking at the color scales, visible improvement going from **b** to **c** is noted.

$\{\lambda_0 = 1.551\mu m\ ; n = 1.507\ ; w_0 = 4\mu m\ ; z_R = 50\mu m\ ; \theta_d = 4.64^0\ ; z_{plot} = 100\mu m(equation\,20)\}$.

---

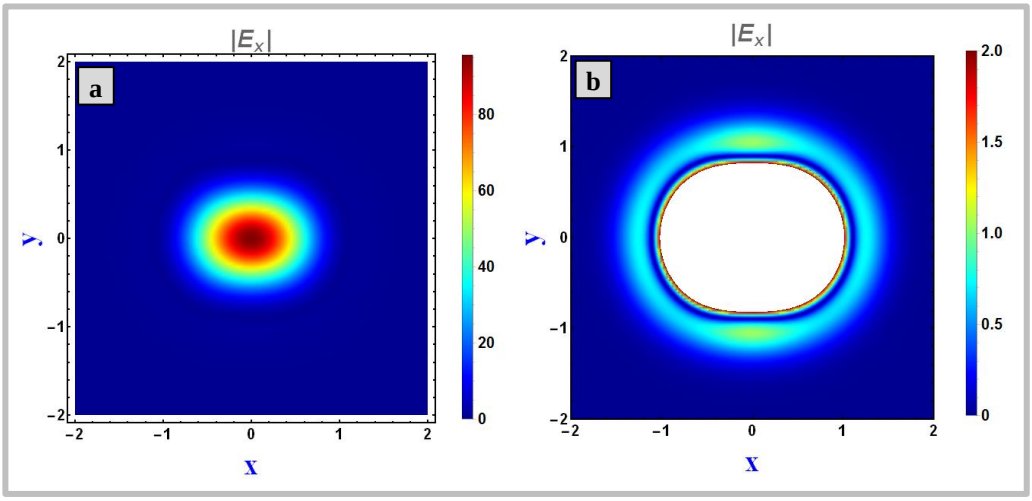


**FIG. S8.** Electric-field $x$-component ($E_x$) at the focal plane of a high divergence-angle Gaussian beam ($\theta_d = 37^0 \Longrightarrow w_0 = 0.5\mu m$), showing a weak ring around the main spot. **a** – full color-scale. **b** – clipped color-scale. The weak ring is clearly visible. Similar rings show up also for the other field components. Note that these rings are predicted by the free-medium analytic expressions and are not a result of a limiting aperture.

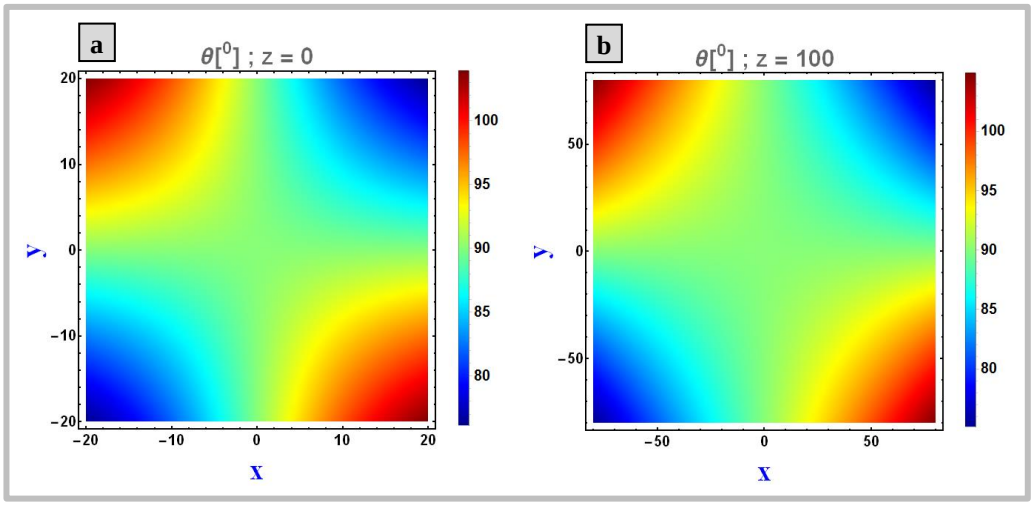


**FIG. S9.** Distribution of angles between the electric field vector and the magnetic field vector of a linearly polarized Gaussian beam. **a** – at the focal plane. **b** – at $z = 100\mu m$. Clearly, the two field vectors of a linearly polarized Gaussian beam are generally not perpendicular to each other, with deviation from perpendicularity increasing with transverse distance from the symmetry axis. On the $x = 0$ and the $y = 0$ planes however, the vectors are perpendicular. Note the change in the span of the $x, y$ coordinates going from **a** to **b**.

## 3. Power conservation – linearly polarized Gaussian beam

The power carried by an electromagnetic field axially propagating through a lossless medium must be conserved. Namely, the total power crossing a plane perpendicular to the propagation direction, say $z$, must be independent of $z$. The time-averaged axial power flow ($P(z)$) is given by integrating the $z$ component of the time averaged Poynting vector ($\boldsymbol{S}_{avg}(x, y, z)$) along the transverse plane:

$$P(z) = \iint_{-\infty}^{\infty} S_{avg,z}(q_1, q_2, z) \cdot dq_1 \cdot dq_2 \qquad \textbf{(S6)}$$

Applying **(S6)** to the field components listed in **TABLE I** we find that the time-averaged power flow carried by the zero-order components is conserved (**a** of **FIG. S10**). However, when the second-order terms are added, we find that power is not conserved. The added second-order components cause the total power to essentially shoot up parabolically with increasing axial distance from the focal plane (**b** of **FIG. S10**).

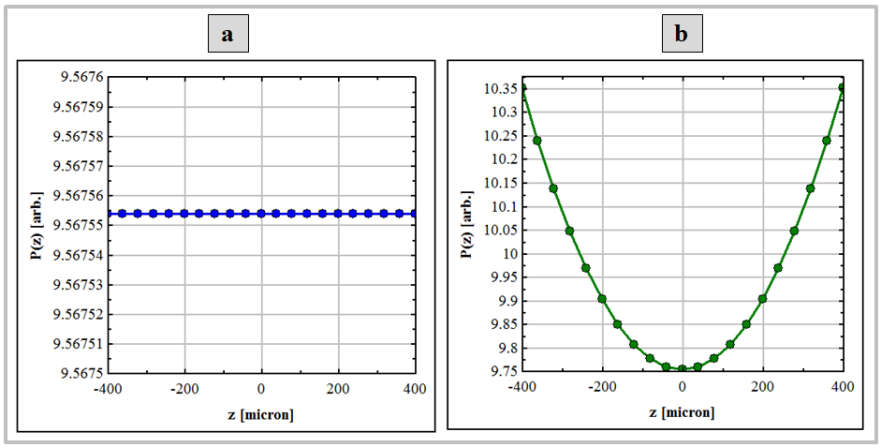


**FIG. S10.** Power conservation by an approximated linearly polarized Gaussian beam. **a** – power carried by a beam described by the zero-order components only. In this case power is strictly conserved at all divergence angles. **b** – power carried by a beam described by adding the second-order components is not conserved.

Power non-conservation by the second-order correction terms is a manifestation of the limited extent in which addition of these terms results in improved accuracy.

The angle-axial distance space where addition of the second-order correction terms results in improved accuracy can be determined by the accuracy of solving Helmholtz equation. Shown by **FIG. S11** is the case of degraded accuracy when the second-order term is added to the expression for the vector potential. So a practical border in angle-axial distance space can be set somewhere between the parameters for **FIG. S7** and the parameters for **FIG. S11**.

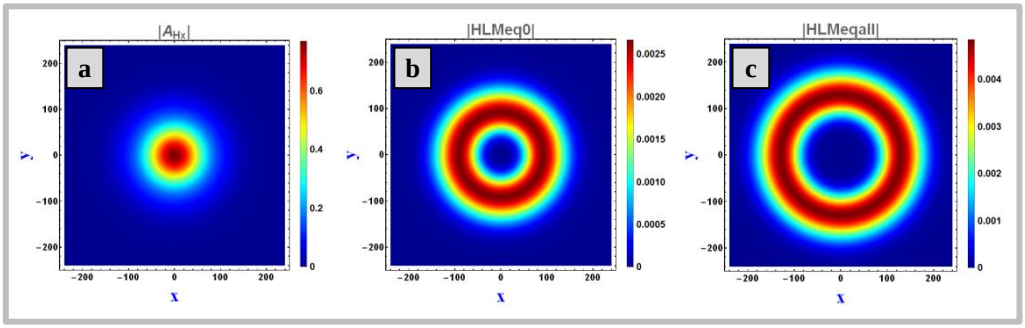


**FIG. S11.** Degraded accuracy of the solution to Helmholtz equation for the vector potential. **a** – map of the two-term single component vector potential (absolute value of). **b** – residue of Helmholtz equation applied to the zero-order vector potential only (top of Eq. **(S4)**). **c** - residue of Helmholtz equation applied to the two orders vector potential (bottom of Eq. **(S4)**). Looking at the color scales, larger residue is seen going from **b** to **c.** At the angle-axial distance for which the maps were calculated (and beyond), addition of the second-order term actually degrades the accuracy of field components' mathematical description.

$\{\lambda_0 = 1.551\mu m\ ; n = 1.507\ ; w_0 = 2\mu m\ ; z_R = 12.5\mu m\ ; \theta_d = 9.28^0\ ; z_{plot} = 400\mu m\}$

The two maps of **FIG. S12** show the axial component of the time-averaged Poynting vector calculated with the parameters used for calculating the maps of **FIG. S11**. Indeed the maps of **FIG. S12** indicate how drastically the accuracy of the Gaussian beam description is degraded at these angle-distance parameters when second-order terms are included.

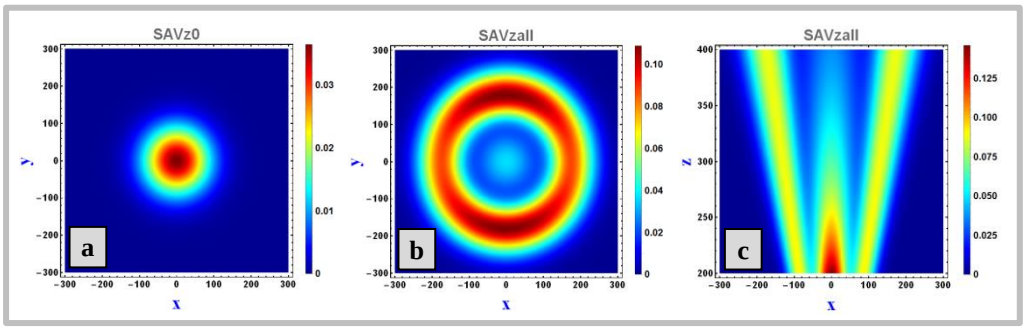


**FIG. S12.** Axial power flow ($S_{avg,z}$). **a** – zero-order expressions only. **b**, **c** – second-order terms included. The **b** and **c** maps indicate the inaccuracy of fields' mathematical description at large angle-distance, due to the addition of second-order expressions. The **b** and **c** maps show a ring-shaped cross-section which is untrue for an $x$-polarized Gaussian beam.
$\{\lambda_0 = 1.551\mu m\ ; n = 1.507\ ; w_0 = 1\mu m\ ; z_R = 3.125\mu m\ ; \theta_d = 18.55^0\ ; z_{plot} = 400\mu m\}$.

Sections **2** and **3** complete our discussion of linearly polarized Gaussian beams. Next - radially polarized Gaussian beams, the Gaussian beams derived from a two-term $z$-polarized vector potential.

## 4. Radially polarized Gaussian fields – illustrating maps

Following are illustrating maps of the radially-polarized field components (derived from a $z$-polarized Gaussian vector potential). Of course radially is a short generic name for radially-azimuthally as, for example, the $\phi$ component of the magnetic field is azimuthally polarized.

The maps of **FIG. S13** and **FIG. S14** show the zero-order (top row) and the second-order (bottom row) spatial distribution of the radially polarized field components, with the parameters (**[48]** Eq. **(20)**). Note that we show absolute value (not absolute value squared). As shown by the color scales, at the selected Gaussian beam parameters, the second-order fields are very weak and the second-order terms do improve the solution accuracy of Helmholtz equation (for the single component vector potential, cf. **FIG. S7**, as well as for the field components).

Next, **FIG. S15** shows power flow of the radially polarized Gaussian beam, as calculated by the time-averaged Poynting vector - $\boldsymbol{S}_{avg}(x, y, z)$ (Eq. **(S3)**). Top row shows cross-sectional maps at $z_{plot} = 100\mu m$ and bottom row shows axial maps in the $r$-$z$ plane.

Last figure in this section, **FIG. S16**, displays a distribution map of the angle between the electric-field vector and the magnetic-field vector. Generally, free-medium electromagnetic waves are not necessarily perpendicular **[46]**. However, in the case of the radially polarized Gaussian beam, the electric-magnetic field vectors are perpendicular at all divergence angles and at all axial distances, including $z = 0$, i.e. including the focal plane.

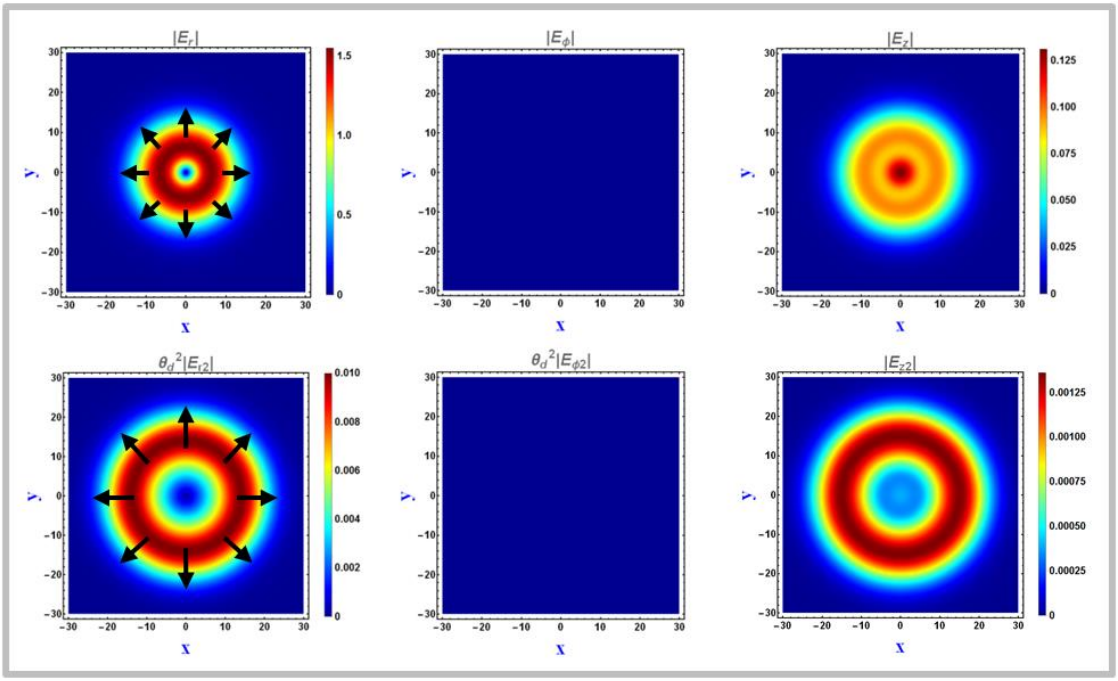


**FIG. S13.** Electric field components of a radially polarized Gaussian beam, derived from a z-polarized Gaussian vector potential (13-18 in **TABLE II**). Top row – full field expressions. Bottom row – corrections only. The maps at the top, with the parameters (**[48]** Eq. **(20)**), are (slightly) more accurate (vs. the zero-order-only maps).

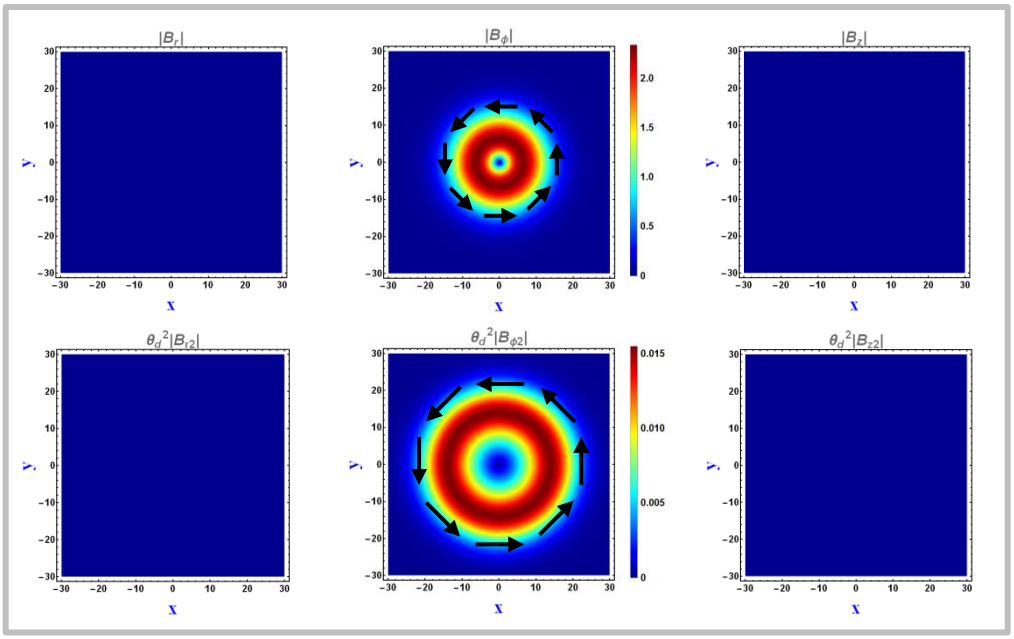


**FIG. S14.** Magnetic field components of a radially polarized Gaussian beam, derived from a z-polarized Gaussian vector potential (19-24 in **TABLE II**). Top row – full field expressions. Bottom row – corrections only. The map at the top row, with the parameters (**[48]** Eq. **(20)**), is (slightly) more accurate (vs. the zero-order-only map).

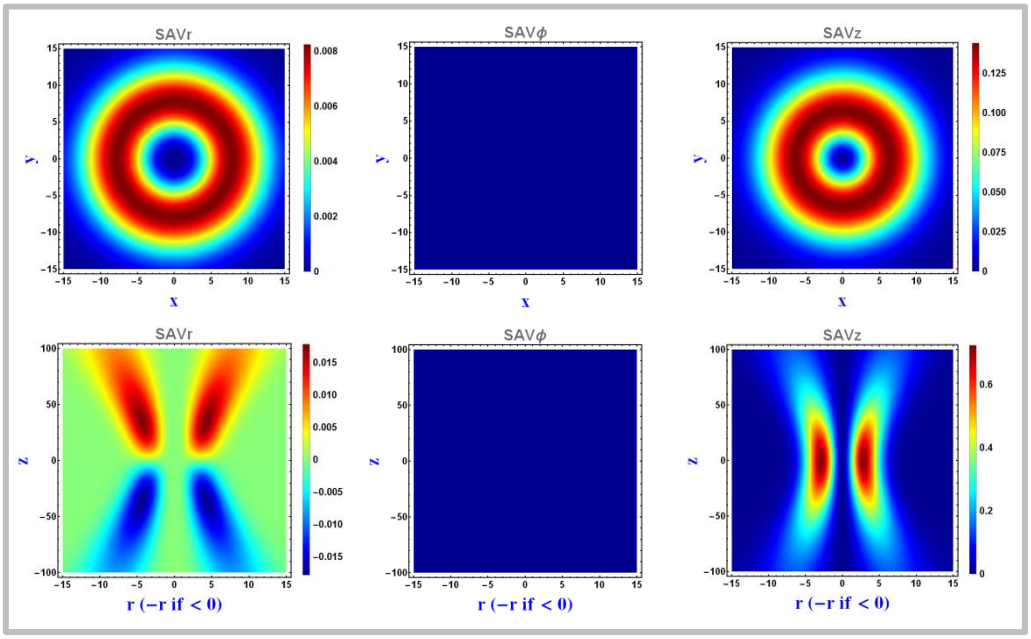


**FIG. S15.** Intensity flow of a radially polarized Gaussian beam ($\boldsymbol{S}_{avg}^{RDL}(x,y,z)$). The maps were calculated for the full field expressions, and thus, at the shown parameter space, are (slightly) more accurate (vs. the zero-order-only maps). Values of color scales calculated for $C_{light} = 1$ (cgs).

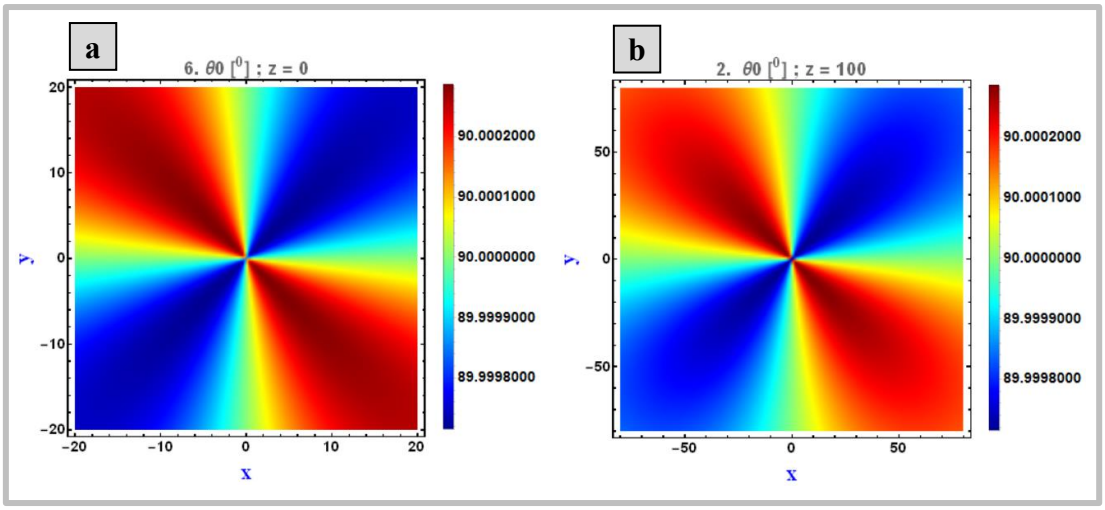


**FIG. S16.** Distribution of angles between the electric field vector and the magnetic field vector of a radially polarized Gaussian beam. **a** – at the focal plane. **b** – at $z = 100\mu m$. As shown, the electric-magnetic field vectors of a radially polarized Gaussian beam are perpendicular to each other. The shown small deviations from $90^0$ are the result of an intentionally introduced small artifact. Note the change in the span of the $x, y$ coordinates going from **a** to **b**.

## 5. Power conservation – radially polarized Gaussian beam

Applying the integrals **(S6)** to the radial fields, we calculated the axial power flow of a radially polarized Gaussian beam - **TABLE II** and **TABLE III**.

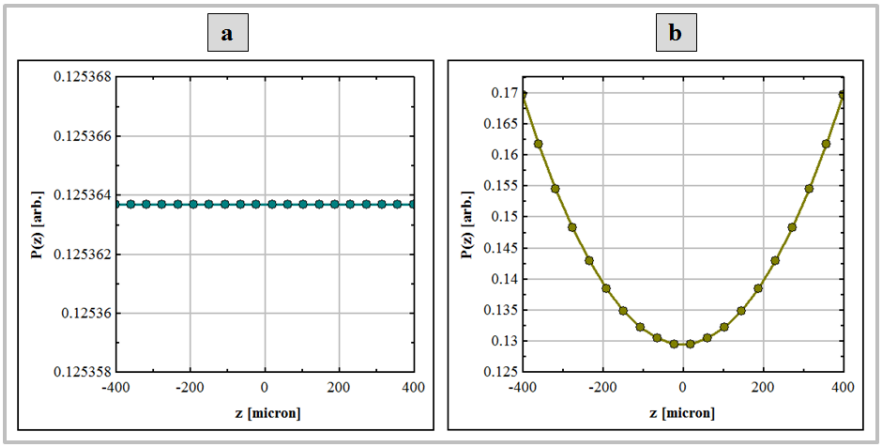


**FIG. S17.** Power conservation by an approximated radially polarized Gaussian beam. **a** – power carried by a beam described by the zero-order components only. In this case power is strictly conserved at all divergence angles. **b** – power carried by a beam described by adding the second-order components is not conserved.

As shown by **FIG. S17**, the time-averaged axial power carried by the beam calculated for the zero-order terms is strictly conserved (**a** of **FIG. S17**). The time-averaged axial power carried by the beam calculated for the zero- and the second-order terms is not conserved (**b** of **FIG. S17**). Looking at **FIG. S10** and at **FIG. S17** we can summarize as follows – when the Gaussian beam is described by zero-order terms only, the axial power flow is strictly conserved for both the linearly polarized beam, and for the radially polarized beam. When second-order terms are added, axial power flow is not conserved. Thus, the use of the second-order terms is allowed only in the small-angles-short-distances parameter space.

## References


**[1]** L. W. Davis, Theory of electromagnetic beams, Phys. Rev. A 19, 1177 (1979).

**[2]** Julius A. Stratton, Electromagnetic Theory (McGraw-Hill Book Company, New York and London, 1941).

**[3]** U. Levy, S. Derevyanko, and Y. Silberberg, Light Modes of Free Space, Progress in Optics, Volume 61, 2016, pp. 237–281

**[4]** M. Lax, W. H. Louisell, and W. B. McKnight, From Maxwell to Paraxial Optics, Phys. Rev. A 11, 1365-1370 (1975).

**[5]** G. P. Agrawal and D. N. Pattanayak, Gaussian beam propagation beyond the paraxial approximation, JOSA 69, 4, 575-578 (1979).

**[6]** D. N. Pattanayak and G. P. Agrawal, Representation of vector electromagnetic beams, Phys. Rev. A 22, 3 (1980).

**[7]** L. W. Davis and G. Patsakos, TM and TE electromagnetic beams in free space, Opt. Lett. 6, 1, (1981) pp. 22-23.

**[8]** W. L. Erikson and Surendra Singh, Polarization properties of Maxwell-Gaussian laser beams, Phys. Rev. E 49, 6 (1994).

**[9]** J. P. Barton and D. R. Alexander, Fifth-order corrected electromagnetic field components for a fundamental Gaussian beam, J. Appl. Phys. 66, (1989) pp. 2800-2802.

**[10]** Y. I. Salamin and Christoph H. Keitel, Electron Acceleration by a Tightly Focused Laser Beam, Phys. Rev. Lett. 88, 9 (2002)

**[11]** Y. I. Salamin, Guido R. Mocken, and Christoph H. Keitel, Electron scattering and acceleration by a tightly focused laser beam, Phys. Rev. Special Topics - Accelerators and Beams, 5, 101301 (2002).

**[12]** Y. I. Salamin, Fields of a radially polarized Gaussian laser beam beyond the paraxial approximation, Opt. Lett. 31, 17 (2006) pp. 2619-2621.

**[13]** Y. I. Salamin, Accurate fields of a radially polarized Gaussian laser beam, New J. of Phys. 8, 133 (2006).

**[14]** Y. I. Salamin, Fields of a Gaussian beam beyond the paraxial approximation, Appl. Phys. B 86, (2007) pp. 319–326.

**[15]** K. T. McDonald, Axicon Gaussian Laser Beams, http://arxiv.org/pdf/physics/0003056.pdf, (2000).

**[16]** G. Bekefi, Diffraction of electromagnetic waves by an aperture in a large screen, J. Appl. Phys. 24, (1953) pp. 1123–1130.

**[17]** A. L. Cullen and P. K. Yu, Complex Source-Point Theory of the Electromagnetic Open Resonator, Proc. R. Soc. Lond. A. 366 (1979) pp. 155-171.

**[18]** C. J. R. Sheppard and S. Saghafi, Electromagnetic Gaussian beams beyond the paraxial approximation, JOSA A 16, 6 (1999) pp. 1381-1386.

**[19]** G. D. Gillen, K. Baughman, and S. Guha, Application of Hertz vector diffraction theory to the diffraction of focused Gaussian beams and calculations of focal parameters, Opt. Express, 17, 3 (2009) pp. 1478-1492.

**[20]** G. D. Gillen, K. Gillen, and S. Guha, Light Propagation in Linear Optical Media (CRC Press, 2013).

**[21]** J.W. Goodman, Introduction to Fourier Optics (The McGraw-Hill Companies, 1988).

**[22]** Hyo-Chang Kim and Y. H. Lee, Hermite–Gaussian and Laguerre–Gaussian beams beyond the paraxial approximation, Opt. Commun. 169, 1–6, (1999) pp. 9–16.

**[23]** A. Ciattoni, B. Crosignani, and P. Di Porto, Vectorial free-space optical propagation: a simple approach for generating all-order nonparaxial corrections, Opt. Commun. 177 (2000) pp. 9–13.

**[24]** H. Guo, J. Chen, and S. Zhuang, Vector plane wave spectrum of an arbitrary polarized electromagnetic wave, Opt. Express 14, 6, (2006) pp. 2095-2100.

**[25]** J. Turunen and A. T. Friberg, Propagation-Invariant Optical Fields, Progress in Optics, 54, (Elsevier B.V, 2009, chapter. 1).

**[26]** A. Doicu and T. Wriedt, Plane wave spectrum of electromagnetic beams, Opt. Commun. 136, 1–2, 1 (1997) pp. 114–124.

**[27]** G. S. Smith, An Introduction to Classical Electromagnetic Radiation, (Cambridge University, 1997).

**[28]** E. Wolf, Electromagnetic diffraction in optical systems, I. An integral representation of the image field, Proc. R. Soc. London Ser. A 253 (1959) pp. 349–357.

**[29]** B. Richards and E. Wolf, Electromagnetic diffraction in optical systems, II. Structure of the image field in an aplanatic system, Proc. R. Soc. London Ser. A 253 (1959) pp. 358–379.

**[30]** P. Debye, Das Verhalten von Lichtwellen in der Na¨he eines Brennpunktes oder einer Brennlinie, Ann. Phys. 30 (1909) pp. 755–776 (in German).

**[31]** P. Varga and P. Török, Focusing of electromagnetic waves by paraboloid mirrors. II. Numerical results, J. Opt. Soc. Am. A 17, 11 (2000) pp. 2090-2095.

**[32]** K. S. Youngworth and T. G Brown, Focusing of high numerical aperture cylindrical-vector beams, Opt. Express 7, 2 (2000) pp. 77-87.

**[33]** M. A. Lieb and A. J. Meixner, A high numerical aperture parabolic mirror as imaging device for confocal microscopy, Opt. Express 8, 7 (2001) pp. 458-474.

**[34]** M. Leutenegger, R. Rao, R. A. Leitgeb, T. Lasser, Fast focus field calculations, Opt. Express 14, 23 (2006).

**[35]** P. Török, P.R.T. Munro, and Em. E. Kriezis, High numerical aperture vectorial imaging in coherent optical microscopes, Opt. Express 16, 2 (2008) pp. 507-523.

**[36]** N. Olivier and E. Beaurepaire, Third-harmonic generation microscopy with focus-engineered beams: a numerical study, Opt. Express 16, 19 (2008) pp. 14703-14715.

**[37]** H. Kang, B. Jia, and M. Gu, Polarization characterization in the focal volume of high numerical aperture objectives, Opt. Express 18, 10 (2010) pp. 10813-10821.

**[38]** M. Gu, Advanced Optical Imaging Theory (Springer, 2013, section 6.5).

**[39]** A.R. Zakharian, P. Polynkin, M. Mansuripur, and J.V. Moloney, Single-beam trapping of micro-beads in polarized light: Numerical simulations, Opt. Expr. 14, 8 (2006) pp. 3660-3676

**[40]** J. A. Stratton and L. J. Chu, Diffraction Theory of Electromagnetic Waves, Phys. Rev. 56 (1939) pp. 99-107.

**[41]** B. Andreas, G. Mana, and C. Palmisano, Vectorial ray-based diffraction integral, JOSA A, 32, 8 (2015) pp. 1403-1424.

**[42]** Hong Luo, Shiyang Liu, Zhifang Lin, and C. T. Chan, Method for accurate description of a radially polarized Gaussian laser beam beyond the paraxial approximation, Opt. Lett. 32, 12 (2007) pp. 1692-1694.

**[43]** A. Yariv and P. Yeh, Optical waves in crystals (John Wiley& Sons, 1984).

**[44]** F. P. Schafer, On Some Properties of Axicons, Appl. Phys. B 39, 1 (1986).

**[45]** H. A. Haus, Waves and fields in optoelectronics (Prentice-Hall, 1984).

**[46]** U. Levy and Y. Silberberg, Free-space nonperpendicular electric–magnetic fields, J. Opt. Soc. Am. 32, 4 (2015) pp. 647-653.

**[47]** James C. Rautio, The Long Road to Maxwell's Equations, IEEE spectrum, December 1 (2014).

**[48]** U. Levy and Y. Silberberg, "Weakly Diverging to Tightly Focused Gaussian Beams: a Single Set of Analytic Expressions", *J. Opt. Soc. Am. A.* **33** :(10) 1999-2009 (2016).